A double-peaked Lyman-α emitter with a stronger blue peak multiply imaged by the galaxy cluster RXC J0018.5+1626

Lukas J. Furtak, Adèle Plat, Adi Zitrin, Micheal W. Topping, Daniel P. Stark, Victoria Strait, Stéphane Charlot, Dan Coe, Felipe Andrade-Santos, Maruša Bradač, et al.

A double-peaked Lyman-α emitter with a stronger blue peak multiply imaged by the galaxy cluster RXC J0018.5+1626

Lukas J. Furtak [iD],[1]★ Adèle Plat,[2] Adi Zitrin [iD],[1] Micheal W. Topping,[2] Daniel P. Stark,[2] Victoria Strait,[3,4] Stéphane Charlot,[5] Dan Coe,[6] Felipe Andrade-Santos,[7] Maruša Bradač,[8,9] Larry Bradley,[6] Brian C. Lemaux [iD][9,10] and Keren Sharon [iD][11]

[1]*Physics Department, Ben-Gurion University of the Negev, PO Box 653, Be'er-Sheva 84105, Israel*
[2]*Steward Observatory, University of Arizona, 933 N Cherry Ave, Tucson, AZ 85721 USA*
[3]*Cosmic Dawn Center (DAWN), Denmark*
[4]*Niels Bohr Institute, University of Copenhagen, Jagtvej 128, DK-2200 Copenhagen N, Denmark*
[5]*Institut d'Astrophysique de Paris, Sorbonne Université, CNRS UMR 7095, 98bis bvd Arago, F-75014 Paris, France*
[6]*Space Telescope Science Institute, 3700 San Martin Drive, Baltimore, MD 21218, USA*
[7]*Center for Astrophysics | Harvard & Smithsonian, 60 Garden Street, Cambridge, MA 02138, USA*
[8]*Department of Mathematics and Physics, University of Ljubljana, Jadranska ulica 19, SI-1000 Ljubljana, Slovenia*
[9]*Department of Physics and Astronomy, University of California, Davis, One Shields Ave., Davis, CA 95616, USA*
[10]*Gemini Observatory, NSF's NOIRLab, 670 N. A'ohoku Place, Hilo, HI 96720, USA*
[11]*Department of Astronomy, University of Michigan, 1085 South University Drive, Ann Arbor, MI 48109, USA*

ABSTRACT

We report the discovery of a double-peaked Lyman-α (Ly α) emitter (LAE) at $z = 3.2177 \pm 0.0001$ in VLT/MUSE data. The galaxy is strongly lensed by the galaxy cluster RXC J0018.5+1626 recently observed in the RELICS survey, and the double-peaked Ly α emission is clearly detected in the two counter images in the MUSE field of view. We measure a relatively high Ly α rest-frame equivalent width (EW) of $\mathrm{EW}_{\mathrm{Ly}\alpha,\,0} = (63 \pm 2)$ Å. Additional spectroscopy with *Gemini*/GNIRS in the near-infrared (NIR) allows us to measure the H β, [O III] $\lambda 4959$ Å, and [O III] $\lambda 5007$ Å emission lines, which show moderate rest-frame EWs of the order of a few $\sim$10–100 Å, an [O III] $\lambda 5007$ Å/H β ratio of 4.8 ± 0.7, and a lower limit on the [O III]/[O II] ratio of >9.3. The galaxy has very blue UV-continuum slopes of $\beta_{\mathrm{FUV}} = -2.23 \pm 0.06$ and $\beta_{\mathrm{NUV}} = -3.0 \pm 0.2$, and is magnified by factors $\mu \sim 7$–10 in each of the two images, thus enabling a view into a low-mass ($M_\star \simeq 10^{7.5}\,\mathrm{M}_\odot$) high-redshift galaxy analogue. Notably, the blue peak of the Ly α profile is significantly stronger than the red peak, which suggests an inflow of matter and possibly very low H I column densities in its circumgalactic gas. To the best of our knowledge, this is the first detection of such a Ly α profile. Combined with the high lensing magnification and image multiplicity, these properties make this galaxy a prime candidate for follow-up observations to search for LyC emission and constrain the LyC photon escape fraction.

Key words: gravitational lensing: strong – ISM: lines and bands – galaxies: clusters: individual: RXC J0018.5+1626 – galaxies: evolution – galaxies: star formation – dark ages, reionization, first stars.

1 INTRODUCTION

The epoch of cosmic reionization (EoR), which took place at $z \sim$ 5–15 (e.g. Stark et al. 2010; Becker et al. 2015; Planck Collaboration XLVII 2016, VI 2020; Bañados et al. 2019; Robertson 2021; Zhu et al. 2021; Bosman et al. 2022), saw one of the last major phase changes of the Universe as almost the entire neutral hydrogen content in the intergalactic medium (IGM) was reionized. The current consensus strongly suggests early star-forming galaxies, and in particular the faint low-mass population, as the sources that drove cosmic reionization (e.g. Bunker et al. 2010; Bouwens et al. 2011, 2015; McLure et al. 2013; Robertson et al. 2013, 2015; Atek et al. 2015; Finkelstein et al. 2015). The physics that govern the emission

of ionizing photons >13.6 eV by star-forming galaxies and, more importantly, their *escape* into the surrounding IGM however remain largely uncertain. Reionizing the entire IGM would require early star-forming galaxies to have escape fractions of ionizing radiation of $f_{\mathrm{esc,\,LyC}} > 0.2$, on average (e.g. Robertson et al. 2013; Naidu et al. 2020). Because of the opacity of the neutral IGM to Lyman-continuum (LyC; $\lambda_0 < 912$ Å) photons (e.g. Madau 1995; Inoue et al. 2014), it is essentially impossible to directly observe LyC emission of galaxies beyond $z \gtrsim 4.5$ (Vanzella et al. 2018). We therefore need to indirectly infer the LyC escape fractions (and other emission properties) of high-redshift galaxies through signatures that *can* be observed out to high redshifts. This is done by studying LyC leakage in low-redshift analogues of high-redshift galaxies, in particular in Lyman-α (Ly α) emitters (LAEs).

The Ly α line originates from a resonant transition in the hydrogen atom. A connection between Ly α and LyC escape can therefore be

expected theoretically. Indeed, Ly α photons scatter less in lower H I column density regions which would also allow for LyC photons to escape (e.g. Dijkstra, Gronke & Venkatesan 2016) and leave an imprint on the Ly α emission line profile (Verhamme et al. 2015; Kakiichi & Gronke 2021). Also, a correlation between high escape fractions and high Ly α equivalent widths (EWs) is indicated by both simulations (e.g. Maji et al. 2022) and observations (e.g. Verhamme et al. 2017; Marchi et al. 2018; Steidel et al. 2018; Izotov et al. 2021; Flury et al. 2022b). Numerous Ly α emitters (LAEs) have been observed at $z > 6$ (e.g. Pentericci et al. 2014, 2018; Schenker et al. 2014; Hu et al. 2019; Fuller et al. 2020; Goto et al. 2021; Endsley et al. 2022; Wold et al. 2022), some of them even with double-peaked Ly α profiles (Hu et al. 2016; Matthee et al. 2018; Songaila et al. 2018; Meyer et al. 2021; Endsley et al. 2022). Note that the latter is perhaps surprising because the blue peak would have a higher chance of being scattered away by the increasingly neutral IGM at high redshifts. However, while the vast majority of confirmed low-redshift LyC leakers observed to date are strong LAEs, the opposite is not necessarily true: even in large samples of strong LAEs at moderate redshifts $z \sim 3$, direct measurements of LyC escape fractions in systematic searches with ultra-deep *Hubble Space Telescope* (*HST*) imaging and ground-based spectroscopy in ultra-violet (UV) wavelengths remain scarce (Bian & Fan 2020) and spurious in many cases (e.g. Fletcher et al. 2019; Pahl et al. 2021). We therefore need to establish more distinct signatures of LyC leakage in LAEs in order to be able to more robustly identify and target LyC emitter candidates at both high and low redshifts (e.g. Zackrisson et al. 2011, 2017; Zackrisson, Inoue & Jensen 2013; Reddy et al. 2016; Izotov et al. 2018, 2021; Schaerer et al. 2018, 2022; Plat et al. 2019; Tang et al. 2019; Pahl et al. 2020; Matthee et al. 2021; Flury et al. 2022a, b; Naidu et al. 2022).

In this work, we present the serendipitous discovery of a unique case of double-peaked Ly α emission from a galaxy at $z \simeq 3.218$. The galaxy is lensed by the galaxy cluster RXC J0018.5+1626 (also known as CL0016+1609 or MACS J0018+1626; e.g. Ebeling et al. 2007) at $z_d \simeq 0.546$, which was recently imaged with *HST* as a part of the *Reionization Lensing Cluster Survey* (RELICS), building on previous *HST* observations (Coe et al. 2019). We therefore dub the galaxy, RXC0018-LAE1. While double-peaked Ly α profiles are commonly observed in LAEs (Leclercq et al. 2017, 2020; Izotov et al. 2018; Matthee et al. 2021; Kerutt et al. 2022; Naidu et al. 2022), RXC0018-LAE1 shows a peculiar Ly α profile with a significantly stronger blue peak, which could indicate low neutral gas covering fractions that could potentially also allow LyC photons to escape. In general, narrow Ly α peak separation (e.g. Izotov et al. 2018) and Ly α escape at the systemic redshift (e.g. Dijkstra et al. 2016; Matthee et al. 2021; Naidu et al. 2022) are also considered strong indicators of LyC leakage, which is why double-peaked Ly α profiles are interesting for the study of LyC escape fractions. In addition, RXC0018-LAE1 appears to be a low-mass, irregular compact star-forming galaxy and thus likely represents an analogue of high-redshift galaxies, in particular the faint low-mass population that drove the reionization of the Universe. These prospects, the double peak with a stronger blue component, together with the high magnification factors and the multiple imaging, make RXC0018-LAE1 particularly interesting for future studies to constrain LyC emission in the EoR.

This work is structured as follows: In Section 2, we present RXC0018-LAE1, data, and observations. In Section 3, we first present near-infrared (NIR) spectroscopy targeting optical emission lines, which are key to the analysis of the double Ly α emission subsequently presented in Section 4. In Section 5, we present an spectral energy distribution (SED) fit to the galaxy. The results are then

summarized in Section 6. Throughout this paper, we adopt a standard flat Λ cold dark matter cosmology with $H_0 = 70 \, \mathrm{km \, s^{-1} \, Mpc^{-1}}$, $\Omega_m = 0.3$, and $\Omega_\Lambda = 0.7$. All magnitudes are quoted in the AB system (Oke & Gunn 1983).

2 TARGET AND OBSERVATIONS

The object studied in this work, RXC0018-LAE1, is a strongly lensed system multiply imaged by the RELICS cluster RXC J0018.5+1626 (RXC0018 hereafter). As can be seen in the left-hand panel of Fig. 1, each of the two counter images, designated as RXC0018-LAE1.1 and RXC0018-LAE1.2, respectively, is composed of one large and bright main component (RELICS IDs 7203 and 7338) and one smaller and fainter companion (RELICS IDs 7202 and 7337), separated by 0.71 arcsec (0.54 arcsec in RXC0018-LAE1.2). According to our lensing model (see Section 2.3), this translates to a physical distance of $\simeq 2.9 \, \mathrm{kpc}$ in the source plane.

The *HST* imaging of RXC0018 comprises mosaics in 10 broad-band filters of the *Advanced Camera for Survey* (ACS) and the *Wide Field Camera Three* (WFC3): *F435W*, *F555W*, *F606W*, *F775W*, *F814W*, *F850LP*, *F105W*, *F125W*, *F140W*, and *F160W*, which are publicly available in the RELICS repository on the Mikulski Archive for Space Telescopes (MAST). In this work, we use the ACS + WFC3 catalogue, also available in MAST, which contains *HST* fluxes obtained with SEXTRACTOR (Bertin & Arnouts 1996) and photometric redshifts computed with the BAYESIAN PHOTOMETRIC REDSHIFTS code (BPZ; Benítez 2000; Coe et al. 2006). We refer the reader to Coe et al. (2019) for the details of data reduction, catalogue assembly, and photometric redshift computation. The *HST* magnitudes and photometric redshifts used in our analysis are shown in Table 1.

The photometric redshift solution from the RELICS catalogue places the main component of both images at roughly the same redshift $z_{phot} \sim 3.45$ within the uncertainties (see Table 1). In each image there is an additional third source (RELICS IDs 7315 and 7495, see Fig. 1) located 2.5 arcsec away from the main component (2.4 arcsec in RXC0018-LAE1.2). While this source has a similar photometric redshift as the main component, the uncertainties make it unclear if this is a companion to the $z \simeq 3.218$ source or if it lies at a somewhat different redshift. Note that if this source indeed lies at the same redshift as RXC0018-LAE1, it would only be $\simeq 9.8 \, \mathrm{kpc}$ away from the main component.

RXC0018 was also observed with the *Multi Unit Spectroscopic Explorer* (MUSE; Bacon et al. 2010) on ESO's *Very Large Telescope* (VLT) under program ID 0103.A-0777(B) (PI: A. Edge). The final reduced and calibrated data cube is publicly available on the ESO Science Archive. It achieves a 5σ-depth of 23.13 mag, has a spatial pixel scale of 0.2 arcsec pix^{-1}, and a spectral resolution of $\Delta\lambda = 1.25 \, \text{\AA}$. Both RXC0018-LAE1.1 and RXC0018-LAE1.2 consistently show a clearly double-peaked strong emission line at $\sim 5125 \, \text{\AA}$ which corresponds to Ly α at $z \simeq 3.217$ (based on the centre between the two peaks; see Verhamme et al. 2018) in the MUSE coverage of RXC0018. While one might consider the possibility that this double-peaked feature might be the Mg II] $\lambda\lambda 2796 \, \text{\AA}, 2803 \, \text{\AA}$ doublet at $z \simeq 0.831$ or the [O II] $\lambda\lambda 3726 \, \text{\AA}, 3729 \, \text{\AA}$ doublet at $z \simeq 0.375$, these possibilities are clearly ruled out by further spectroscopic analysis (see Section 3) and the lensing configuration. We note that there also exist *Magellan Clay Telescope/Low Dispersion Survey Spectrograph* (LDSS3-C) observations of RXC0018-7203 taken on 2017 July 27 (PI: K. Sharon; for more details see Mahler et al. 2019) but the resolution is insufficient to resolve the double-peak. A detailed
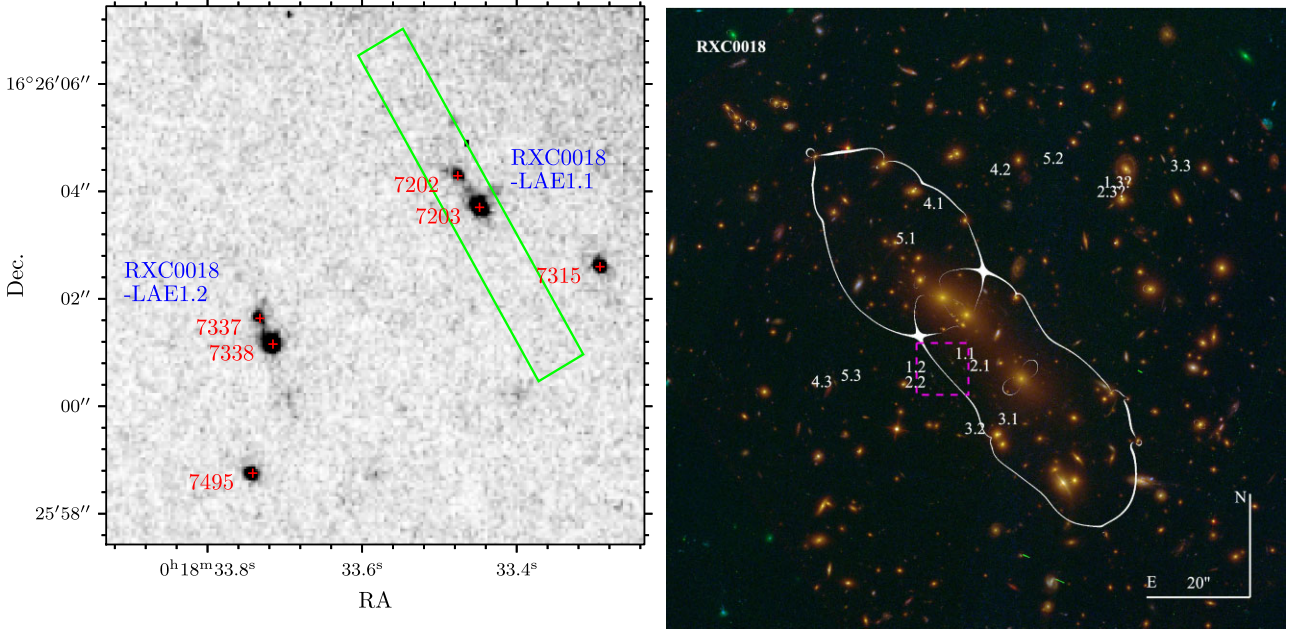
Figure 1. *Left-hand panel*: Centre positions and RELICS catalogue IDs (red) of each component of RXC0018-LAE1 over a stack of all 10 RELICS *HST* images of RXC0018 (see Table 1) in 0.06 arcsec pixel^{-1} resolution. The green rectangle outlines the slit position and orientation used in our GNIRS observations presented in Section 2.2. The relative size of the MUSE detection can be seen in Fig. 3. *Right-hand panel*: Colour image of RXC0018 from the RELICS *HST* data. Numbered on the figure are multiple image families used as constraints for the modelling. Also shown in white are the critical curves for RXC0018-LAE1 (system 1 in the figure) at $z = 3.218$. Additional counter images for systems 1 (RXC0018-7203 and RXC0018-7338) and 2 (RXC0018-7315 and RXC0018-7495) are expected on the other side of the cluster but not yet securely identified in the data. The magenta square represents the 10 arcsec $\times$ 10 arcsec cut-out shown in the left-hand panel.

Table 1. Coordinates, photometric redshifts, gravitational-lensing magnifications, and broad-band photometry of RXC0018-LAE1. The positions, photometric redshifts, and *HST* photometry are taken from the public RELICS catalogue available on MAST and presented in Coe et al. (2019). The extraction of the *K*-band photometry is detailed in Section 2.1 and the magnifications are computed from our best-fitting lensing model presented in Section 2.3.

| RELICS ID | RXC0018-LAE1.1 | | | RXC0018-LAE1.2 | | |
	7203	7202	7315	7338	7337	7495
RA	0^{h}18^{m}33^{s}450	0^{h}18^{m}33^{s}478	0^{h}18^{m}33^{s}294	0^{h}18^{m}33^{s}717	0^{h}18^{m}33^{s}734	0^{h}18^{m}33^{s}743
Dec.	16°26′03″710	16°26′04″297	16°26′02″606	16°26′01″165	16°26′01″645	16°25′58″763
z_{phot}	$3.48^{+0.07}_{-0.08}$	$3.40^{+0.15}_{-3.30}$	$3.28^{+0.12}_{-3.23}$	$3.42^{+0.05}_{-0.09}$	$0.06^{+3.25}_{-0.02}$	$0.29^{+3.26}_{-0.03}$
μ	6.5 ± 0.2	6.6 ± 0.2	4.2 ± 0.1	10.1 ± 0.7	9.7 ± 0.6	6.4 ± 0.4
F435W	25.64 ± 0.11	26.70 ± 0.24	25.93 ± 0.18	25.50 ± 0.08	26.33 ± 0.14	26.43 ± 0.15
F555W	24.60 ± 0.03	26.21 ± 0.08	25.71 ± 0.06	24.53 ± 0.02	26.31 ± 0.08	25.78 ± 0.05
F606W	24.60 ± 0.03	26.32 ± 0.18	25.48 ± 0.04	24.55 ± 0.03	26.05 ± 0.08	25.76 ± 0.06
F775W	24.58 ± 0.03	26.10 ± 0.09	25.56 ± 0.06	24.61 ± 0.03	26.27 ± 0.10	25.59 ± 0.06
F814W	24.59 ± 0.03	26.24 ± 0.08	25.57 ± 0.04	24.56 ± 0.02	26.20 ± 0.07	25.69 ± 0.04
F850LP	24.40 ± 0.06	26.10 ± 0.17	25.83 ± 0.15	24.73 ± 0.07	26.52 ± 0.23	25.43 ± 0.10
F105W	24.81 ± 0.06	26.35 ± 0.17	25.81 ± 0.11	24.92 ± 0.07	26.37 ± 0.16	26.03 ± 0.12
F125W	24.94 ± 0.13	26.06 ± 0.23	25.89 ± 0.21	25.16 ± 0.14	27.37 ± 0.59	26.06 ± 0.22
F140W	24.84 ± 0.10	26.50 ± 0.27	26.17 ± 0.22	25.11 ± 0.11	27.35 ± 0.49	26.01 ± 0.18
F160W	24.94 ± 0.07	26.31 ± 0.16	26.11 ± 0.14	25.01 ± 0.07	26.44 ± 0.17	26.02 ± 0.12
Ks	24.88 ± 0.22^a	26.30 ± 0.61^a	25.89 ± 0.44^a	24.40 ± 0.20	25.88 ± 0.61	25.43 ± 0.43

*Note.^{a}*The *Ks*-band photometry of RXC0018-LAE1.1 was not measured directly but inferred from the RXC0018-LAE1.2 fluxes using the magnification ratio.

analysis of the double-peaked Ly α emission feature of RXC0018-LAE1 seen in the MUSE data is presented in Section 4.

2.1 Ancillary *Ks*-band photometry

In addition to the RELICS photometry, we also use *Ks*-band imaging data taken with the *High Acuity Wide field K-band Imager* (HAWK-I;

Kissler-Patig et al. 2008) on VLT. The *Ks*-band imaging of RXC0018 (Program ID: 0103.A-0871(B), PI: A. Edge) is publicly available on the ESO Science archive and achieves a 5σ-depth of 26.15 mag on a 0.11 arcsec pix^{-1} scale.

We use the PHOTUTILS package (v1.3.0; Bradley et al. 2021) to extract the *K*-band photometry of our target. We subtract a 2D global background and then measure the flux in circular apertures

of diameter $D_{ap} = 0.5$ arcsec around our sources. The fluxes and their uncertainties are then corrected for aperture losses as $f_{tot} = cf_{ap}$, where $c = 1.98$ is the aperture correction factor computed for a 0.5 arcsec aperture from the HAWK-I point spread function (PSF) in Furtak et al. (2021). The resulting *K*-band magnitudes for RXC0018-7338, RXC0018-7337, and RXC0018-7495 are shown in Table 1. We discard the *K*-band photometry for the other image, RXC0018-LAE1.1, because we suspect it to be contaminated by some diffuse noise or possibly foreground source. This consistently also affects, e.g. the *F*850*LP* band in the *HST* imaging (Table 1) and the MUSE data (Section 4.1).

2.2 Gemini GNIRS observations

In order to complement the existing optical MUSE spectroscopy and to precisely measure our target's systemic redshift, we observed RXC0018-7203 and RXC0018-7202 in the NIR range with the *Gemini Near-Infrared Spectrograph* (GNIRS) on the Gemini-North telescope (Program ID: GN-2021B-Q-903; PI: A. Zitrin). Using the 110.5 l/mm grating and the short blue camera in cross-dispersed mode and a slit of length 7 arcsec and width 1 arcsec, we obtained a total of 2 h integration time on target. The slit position and orientation of this observation are also shown in Fig. 1.

The data were reduced, co-added, extracted, and corrected for telluric line absorption with the Gemini IRAF package v1.14.[1] The orders of the cross-dispersed data were then separated into *J*-, *H*-, and *K*-band spectra, respectively, and flux-normalized to the broad-band photometry in each band given in Table 1. Because the GNIRS observations were targeted at RXC0018-LAE1.1 and we only have usable *K*-band photometry for RXC0018-LAE1.2, as explained in Section 2.1, we use the ratio between the magnifications (see Section 2.3 and Table 1) to convert the RXC0018-7338 *K*-band flux to RXC0018-7203. Note that we also apply a heliocentric correction of $-11.3 \, \mathrm{km \, s^{-1}}$ to the spectra, to match the heliocentric-corrected MUSE data frame of reference. The final spectra have (observed) spectral resolutions of $\Delta\lambda = 1.1$ Å, $\Delta\lambda = 1.4$ Å, and $\Delta\lambda = 1.8$ Å, respectively, in the *J*, *H*, and *K* bands.

2.3 Lensing magnification

We construct a strong lensing (SL) model for RXC0018 using the Light-Traces-Mass method (LTM; Zitrin et al. 2009, 2015). We adopt five multiple image systems spanning a redshift range up to $z \sim 5$. The resulting critical curves for our model are shown in the right-hand panel of Fig. 1 together with the multiple image systems used as constraints. A first SL model for this cluster was published by Zitrin et al. (2011) when analysing the 12 $z > 0.5$ MACS clusters (Ebeling et al. 2007). Due to RELICS data, we are able to identify several new sets of multiple image systems and measure photometric redshifts for them (in addition to RXC0018-LAE1 for which there is a spectroscopic measurements). We did not detect any emission lines for the other systems in the MUSE data cube. We use a positional uncertainty of 0.5 arcsec for multiple images in the modelling. The resulting best-fitting model's image reproduction error is 0.86 arcsec. The SL magnifications for the sources analysed in this work are given in Table 1.

We note also that there is another parametric SL model for RXC0018 publicly available on the MAST archive, constructed with
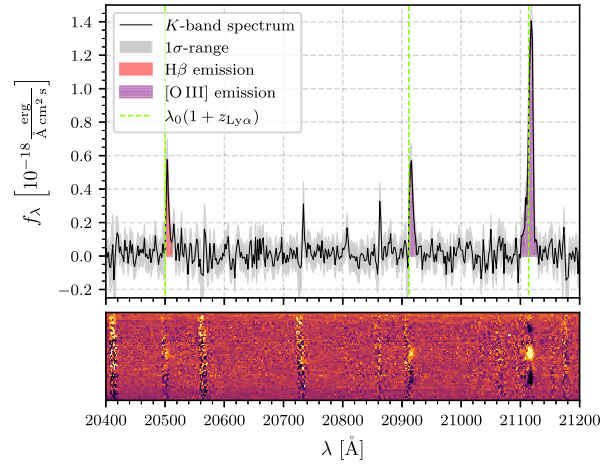
Figure 2. Observed GNIRS *K*-band spectrum of RXC0018-7203 (black) and its 1σ-range (grey shaded area). The three prominent emission features are identified as H β, [O III] λ4959 Å, and [O III] λ5007 Å, respectively. The red and purple shaded areas represent the integrated line fluxes and the green dashed lines show where the respective emission line can be expected according to the Ly α redshift derived from the MUSE data in Section 2).

the SL modelling software LENSTOOL (Kneib et al. 1996; Jullo et al. 2007; Jullo & Kneib 2009). This model seems to predict somewhat higher magnifications at the coordinates of RXC0018-LAE1 than our LTM models (by factors up to $\sim$2). While we do not use this model here and defer a proper comparison of the lens models and their magnifications for future work, we note that higher magnifications would mean the absolute flux results of this work, i.e. integrated fluxes, luminosities, and stellar mass, might be lower.

3 SYSTEMIC REDSHIFT FROM OPTICAL EMISSION LINES

Our GNIRS observations yielded *J*-, *H*- and *K*-band spectra for RXC0018-7203 and RXC0018-7202 covering wavelengths from 12 055 to 13 230 Å, 15 070 to 16 480 Å, and 20 085 to 21 965 Å, respectively. While we do not find any significant emission in the *J* and *H* bands, our *K*-band spectrum shows three strong emission features as can be seen in Fig. 2. These are consistent with the optical [O III] doublet, [O III] λ5007 Å, and [O III] λ4959 Å, and the H β-line at the redshift expected from the MUSE and photometric data (see Section 2). We use the SPECUTILS package (v1.5.0; Earl et al. 2021) to perform a Gaussian fit to each emission line and thus obtain line centroids and widths. In order to accurately propagate the pixel-wise variance of the data to the line parameters, we evaluate the joint posterior distribution of 20 *Monte Carlo Markov Chains* (MCMC) of 10^4 steps each, run with the EMCEE package (Foreman-Mackey et al. 2013), and compute the uncertainties of each fit-parameter. We integrate the observed spectrum at each emission line to obtain line fluxes as shown by the shaded areas in Fig. 2 and correct them for magnification. The wavelength window for the flux integration is chosen using the 99.7 per cent-range (3σ) of the Gaussian fit to each line. All measured properties of the emission lines are summed up in Table 2.

Using the centroids of the Gaussian fits to the three optical emission lines and the associated uncertainties, we find a weighted average systemic redshift of $z_{sys} = 3.2177 \pm 0.0001$ for RXC0018-7203. These clear detections of the rest-frame optical lines in the *K*-band spectrum further rule out the lower redshift Mg II] or [O II]

Table 2. GNIRS rest-frame optical spectroscopy results for RXC0018-7203. The integrated line fluxes were corrected for gravitational magnification given in Table 1.

Line	λ_0 [Å]	λ_{obs} [Å]	z	FWHM [Å]	FWHM [km s^{-1}]	F_{line} [10^{-18} erg s^{-1} cm^{-2}]	EW$_{obs}$ [Å]	EW$_0$ [Å]
Hβ	4861.333[a]	20504.0 ± 0.8	3.2178 ± 0.0002	6.3 ± 1.4	92 ± 30	0.42 ± 0.06	140 ± 49	33 ± 12
[O III]λ4959 Å	4958.911[a]	20915.2 ± 1.0	3.2177 ± 0.0002	9.0 ± 1.5	130 ± 32	0.56 ± 0.05	187 ± 62	44 ± 15
[O III]λ5007 Å	5006.843[a]	21117.4 ± 0.2	3.2177 ± 0.0001	8.0 ± 0.6	114 ± 15	2.00 ± 0.10	672 ± 217	159 ± 51

Note. [a]Taken from the NIST Atomic Spectra Database, available at https://physics.nist.gov/asd. Note that quoted here are air wavelengths.

doublet scenarios for the double-peaked emission line in the MUSE spectra and firmly confirm it to indeed be the Ly α line. Note that we do not observe any significant spatial offset that could correspond to the separation of RXC0018-7203 and RXC0018-7202 in the *HST* imaging (see Fig. 1 and Section 2). The separation of 0.71 arcsec is however at the limit of the spatial resolution obtained in our GNIRS (0.15 arcsec pixel^{-1}) observations given the average seeing of $\sim$0.7 arcsec (varying between $\sim$0.5 and $\sim$1 arcsec over the 2 h of observations). We therefore conclude that RXC0018-7202 either does not contribute significant flux to the measured emission lines, which is plausible given its faintness ($\sim$26 mag) in the *K* band, or it is indistinguishably blended into the line emission of RXC0018-7203.

We compute the optical line EWs using the *K*-band flux shown in Table 1 and taking the magnification ratio into account as explained in Section 2.2. As can be seen in Table 2, we find relatively low optical EWs of order EW$_0$ $\sim$ 10–100 Å in RXC0018-7203 which sets RXC0018-LAE1 slightly apart from objects typically used as high-redshift analogues, such as e.g. extreme emission line galaxies (EELGs) with [O III] EWs $\gtrsim$ 1000 Å (e.g. Atek et al. 2011, 2014; Maseda et al. 2014, 2018; Reddy et al. 2018b; Jaskot et al. 2019; Tang et al. 2019; Boyett et al. 2022) or 'Green Pea' galaxies which also typically display very strong optical emission lines (e.g. Cardamone et al. 2009; Izotov, Guseva & Thuan 2011; Amorín et al. 2012; Jaskot & Oey 2013; Henry et al. 2015). Optical emission lines with low EWs on the other hand could however be an indication of LyC escape as was found by Zackrisson et al. (2013, 2017): According to these works, EW$_{H\beta, 0}$ $\lesssim$ 30 Å in particular would imply LyC escape fractions $f_{esc, LyC}$ $\gtrsim$ 0.5.

We also find an [O III] λ5007 Å/H β ratio of 4.8 ± 0.7 which is relatively high for a star-forming galaxy but slightly lower than the ratios typically found in EELGs (e.g. Tang et al. 2019). We do not detect any emission from the [O II] $\lambda\lambda$3726 Å,3729 Å doublet in the *H*-band spectrum with a magnification-corrected 3σ upper limit of < 0.22 × 10^{-18} erg s^{-1} cm^{-2} (see Appendix A1). This results in a 3σ lower limit on the [O III]/[O II] λ3726 Å+3729 Å ratio of >9.3. Note that high [O III]/[O II] ratios have been found to correlate with LyC leakage (Izotov et al. 2016; Izotov, Thuan & Guseva 2017; Izotov et al. 2018; Fletcher et al. 2019; Jaskot et al. 2019; Flury et al. 2022b) but do not necessarily represent a sufficient condition for high LyC escape fractions (Stasińska et al. 2015; Shapley et al. 2016; Izotov et al. 2018; Naidu et al. 2018; Bassett et al. 2019; Jaskot et al. 2019; Plat et al. 2019; Tang et al. 2019).

4 DOUBLE-PEAKED LYMAN ALPHA

With the systemic redshift in hand, we can confirm that the double-peaked emission feature detected in the MUSE data is indeed the Ly α line at $z = 3.218$. Note that we also tentatively detect other rest-frame UV emission lines in the MUSE data of RXC0018-LAE1 as detailed in Appendix A2. These are however relatively weak and we therefore defer more detailed analysis to future work.

Fig. 3 shows MUSE signal-to-noise contours of the two Ly α components. In both images the Ly α emission is consistently centred on the main component, i.e. RXC0018-7203 and RXC0018-7338, respectively. This rules out the possibility of the double peak arising from a separate Ly α emission from the secondary component at a slightly different redshift and instead confirms that the double peak is therefore genuine and originates from the same region in space. The figure also clearly shows that both the blue and the red Ly α emission have fairly similar and symmetric morphologies. Since gravitational lensing is achromatic, this means both peaks are equally affected by possible differential magnification due to the proximity with the
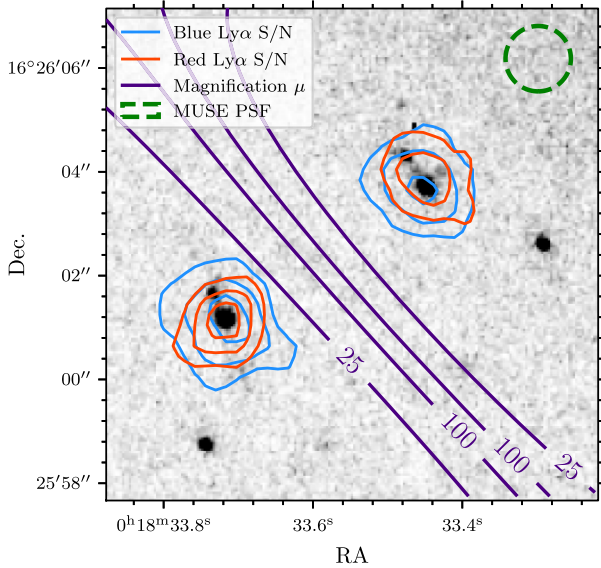
Figure 3. MUSE S/N-contours at $\lambda = 5122.6$ Å (blue) and $\lambda = 5128.9$ Å (red), corresponding to the two Ly α peaks of RXC0018-LAE1 over the same RELICS *HST* image stack as in Fig. 1. The blue contours are computed from a stack of four elements on the spectral axis and the red contours from a stack of three spectral elements around the central wavelength. The contours represent, from outer to inner, 2σ, 3σ, and 4σ. Note that in both images both Ly α peaks are centred on the main component of the *HST* imaging. We show gravitational magnification contours for a source at $z = 3.218$ according to our LTM model (see Section 2.3) as dark blue lines. The critical line passes right between the two images RXC0018-LAE1.1 and RXC0018-LAE1.2. The green circle represents the FWHM of the MUSE PSF (1.25 arcsec).

critical line which passes in between the two images, RXC0018-LAE1.1 and RXC0018-LAE1.2 as is also shown in Fig. 3. We can therefore safely ignore differential magnification effects in the analysis of this galaxy's Ly α profile.

Recent studies have revealed that LAEs commonly have Ly α haloes of relatively low surface brightness which extend far beyond, up to 10 ×, the spatial extent of the stellar continuum emission detected in broad-band photometry (e.g. Hayashino et al. 2004; Steidel et al. 2011; Momose et al. 2014, 2016; Wisotzki et al. 2016; Leclercq et al. 2017; Cai et al. 2018; Wisotzki et al. 2018; Cantalupo et al. 2019; Leclercq et al. 2020). Since the halo typically represents ~ 65 per cent of the total Ly α emission (Leclercq et al. 2017), we need to take special care in the extraction to include *all* of the Ly α flux as detailed in the next section.

4.1 Ly α flux extraction

In order to extract all the Ly α flux of our sources and account for the emission in the low-surface-brightness halo, we follow the approach generally established for this kind of study with MUSE data (e.g. Wisotzki et al. 2016; Drake et al. 2017a, b; Hashimoto et al. 2017; Leclercq et al. 2017; Kerutt et al. 2022). We first use the SPECTRAL-CUBE package (v0.2; Ginsburg et al. 2014) to cut out a 16 arcsec × 16 arcsec region that encompasses both images of RXC0018-LAE1 on the two spatial axes and then use a median filter of 200 pixels on the spectral axis (250 Å) to construct a continuum-only cube. The spectral window used for the filter has been found to effectively remove emission lines in MUSE data (Herenz & Wisotzki 2017). We then subtract the continuum cube from the original 16 arcsec × 16 arcsec cube and construct three narrow-band (NB) images: a total
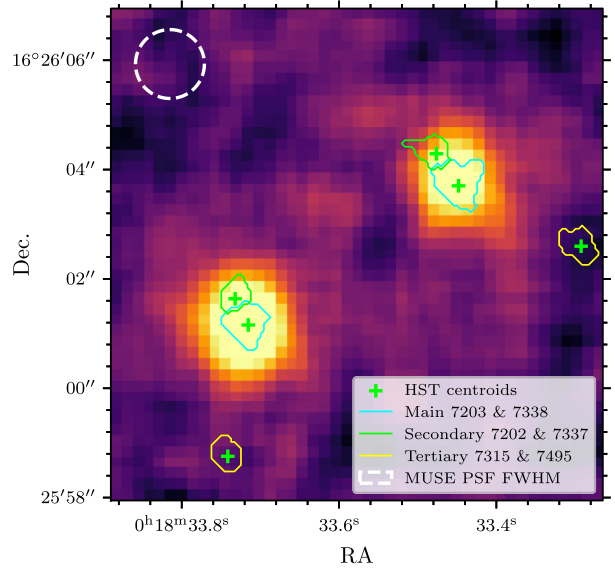

Figure 4. Continuum-subtracted full Ly α (15 Å) NB image of RXC0018-LAE1 smoothed with a 2D Gaussian kernel of $\sigma = 0.5$ arcsec. The green crosses represent the coordinates of the RELICS *HST* detections and the white dashed circle the FWHM of the MUSE PSF. The solid contours represent the segmentations of the RELICS *HST* detections.

NB image encompassing the total Ly α emission, one centred on the blue peak, and one on the red peak. Note that we find residual continuum at the position of RXC0018-LAE1.1 in the continuum-subtracted cube. We therefore adopt the flux measurements of the counter image RXC0018-LAE1.2 as fiducial results in the following text.

The NB images have bandwidths of 15 Å for the total Ly α NB image and 7 and 8 Å each for the blue and red NB images, respectively. These were chosen as the limits where the continuum-subtracted MUSE flux density crosses zero on either side of the double-peaked Ly α emission. The total Ly α NB image of RXC0018-LAE1 is shown in Fig. 4. We use PHOTUTILS (see Section 2.1) to measure the centroids and kron radii (Kron 1980) of the Ly α emission on both multiple images. Consistently in both RXC0018-LAE1.1 and RXC0018-LAE1.2, the centroids of the blue and the red peak align with the total Ly α peak and the RELICS catalogue coordinates within $\lesssim 0.1$ arcsec. This further confirms that the total Ly α emission of RXC0018-LAE1 originates from its main component and thus that the double peak is genuine.

Finally, continuum-subtracted spectra are extracted in a circular aperture of three Kron radii around the total Ly α centroids and collapsed to 1D-spectra. The chosen aperture size has been found to reliably extract Ly α halo fluxes as discussed extensively in Kerutt et al. (2022). We integrate the obtained spectra in the bandwidth of the total Ly α NB image to obtain total Ly α fluxes for both images.

4.2 UV continuum

In order to compute the Ly α EW of RXC0018-LAE1, we measure the continuum following the method detailed in Hashimoto et al. (2017) and fit a power-law relation

$$m(\lambda) = -2.5 \log(\lambda^{\beta+2}) + m_0, \qquad (1)$$

where β is the UV-continuum slope and m_0 a constant to the rest-frame UV photometry. We fit this relation for the main component of RXC0018-LAE1.2, RXC0018-7338, because of the possible
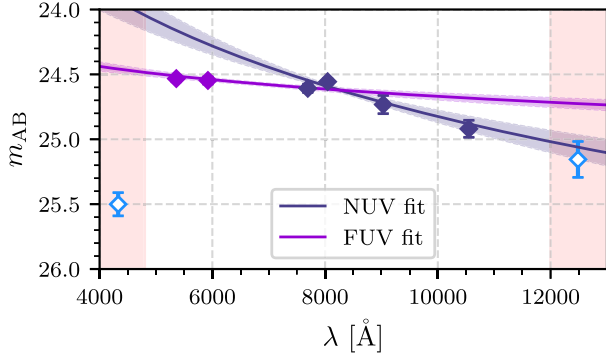
Figure 5. Power-law fits to the rest-frame UV photometry of RXC0018-7883. The dark purple line represents our NUV fit ($\lambda_0 = 1700$–2400 Å, dark purple points) and the light purple line the FUV fit to the same bands in addition to the two bluer filters (light purple points). The adjacent filters, not used in either fit, are shown as open blue points. The red shaded areas delimit the full $\lambda_0 = 1100$–2400 Å range used in the FUV fit.

foreground contamination in RXC0018-LAE1.1 mentioned in Sections 2.1 and 4.1. Because there appears to be a flattening of the UV continuum towards the two bluer filters (see Table 1), we fit the continuum twice: one near UV (NUV) continuum spanning a rest-frame wavelength range from 1700 to 2400 Å (filters $F775W$, $F815W$, $F850LP$, and $F105W$) as in e.g. Bouwens et al. (2009), Hashimoto et al. (2017), and a far-UV (FUV) continuum including the two bluer filters $F606W$ and $F555W$, i.e. down to rest-frame 1100 Å. The fits are performed with 20 MCMC chains of 10^4 steps each. Both fits are shown in Fig. 5. The resulting UV-slopes are both very blue which indicates a very low dust attenuation and might also indicate possible LyC escape (e.g. Zackrisson et al. 2013, 2017, also see discussion in Section 5). Interestingly, we find a marked difference between the FUV and NUV slopes $\beta_{\rm FUV} = -2.23 \pm 0.06$ and $\beta_{\rm NUV} = -3.0 \pm 0.2$.

Using this UV-continuum fit, we infer the flux density at rest-frame 1500 Å and from that compute the absolute UV magnitude of the main component of RXC0018-LAE1 which yields $M_{\rm UV} = -18.58 \pm 0.07$.

4.3 Ly α EW and emission profile

We measure a total magnification-corrected integrated Ly α flux of $F_{\rm Ly\alpha} = (17 \pm 1) \times 10^{-18}$ erg s^{-1} cm^{-2} which yields a relatively high Ly α luminosity of $L_{\rm Ly\alpha} = (6.7 \pm 0.5) \times 10^{42}$ erg s^{-1} cm^{-2} for RXC0018-LAE1. Using the rest-frame UV-continuum fit obtained in Section 4.2 to infer the continuum at Ly α, this results in a rest-frame EW of $\rm EW_0 = (63 \pm 2)$ Å.

The continuum-subtracted 1D-spectra of the two multiple images are shown in Fig. 6. They clearly display the double-peaked nature of the Ly α emission of RXC0018-LAE1. We fit the two peaks to obtain line centres and widths with the same method as for the optical emission lines in Section 3 and find line widths of $\rm FWHM_{blue} = (179 \pm 37)$ km s^{-1} and $\rm FWHM_{red} = (211 \pm 41)$ km s^{-1}. The two Gaussian fits for RXC0018-7338 are shown in Fig. 7. We also note a pronounced asymmetry in velocity space with regard to the systemic redshift: While the two peaks are separated by $\Delta v = (376 \pm 32)$ km s^{-1}, the red peak lies much closer, $\Delta v_{\rm red} = (83 \pm 11)$ km s^{-1}, to the systemic redshift than the blue peak which is shifted much further by $\Delta v_{\rm blue} = (-293 \pm 10)$ km s^{-1}. Recently, Verhamme et al. (2018) measured a correlation between the peak separation Δv, red peak shift $\Delta v_{\rm red}$ from the systemic velocity, and the (red-peak) Ly α FWHM in double-peaked LAEs. RXC0018-LAE1
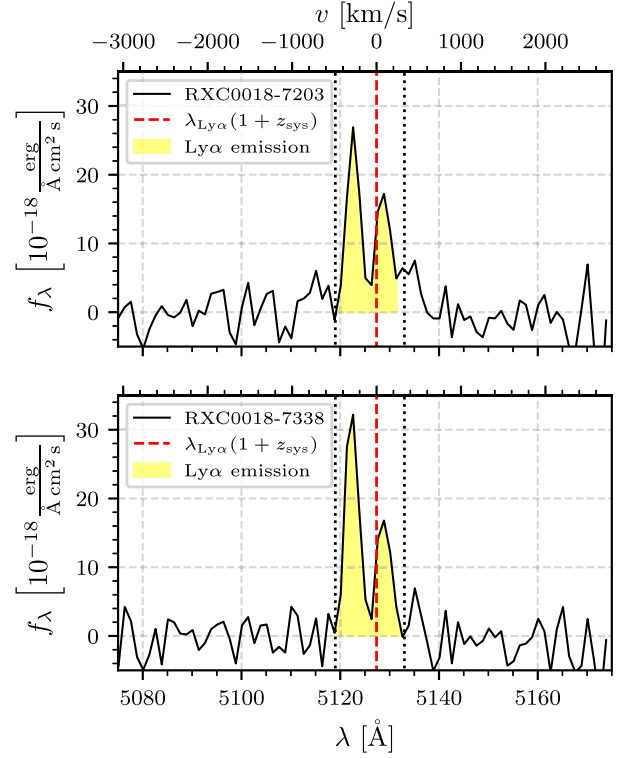

Figure 6. Continuum-subtracted Ly α emission in RXC0018-LAE1.1 (upper panel) and its counter image RXC0018-LAE1.2 (lower panel) with the systemic redshift marked as the red dashed line. The uncertainty of the systemic redshift is too small to be visible in the figure. Unlike other double-peaked LAEs observed to date, the blue peak is significantly stronger than the red peak and the two peaks show asymmetric shifts in velocity space. The yellow shaded area represents the total integrated Ly α flux and the black dotted lines the bandwidth of the Ly α NB image (see Section 4.1).
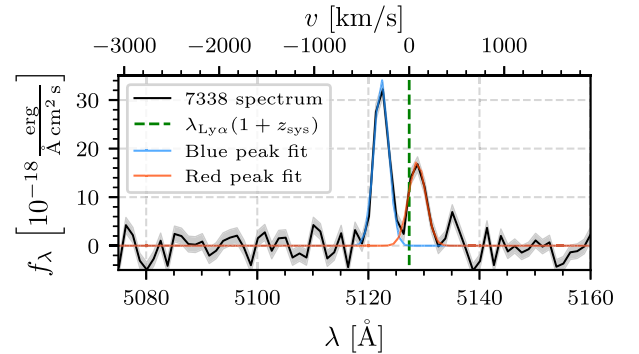

Figure 7. Continuum-subtracted Ly α emission of RXC0018-LAE1.2 with its 1σ-range (grey shaded area) and the systemic redshift marked as the green dashed line. The two Gaussian fits to the two Ly α peaks are shown as blue and red lines, respectively.

significantly deviates (by $>2\sigma$) from the first of these relations with $\Delta v_{\rm red}(\Delta v) = (185 \pm 43)$ km s^{-1} inferred by the peak separation. The second one however, $\Delta v_{\rm red}(\rm FWHM_{red}) = (156 \pm 77)$ km s^{-1} computed using the FWHM of the red peak, agrees by $\sim 1\sigma$ with our measured red peak shift from the systemic velocity. Note that the uncertainties on all of our velocity measurements are relatively large due to the low spectral resolution of MUSE which might in part explain these deviations.
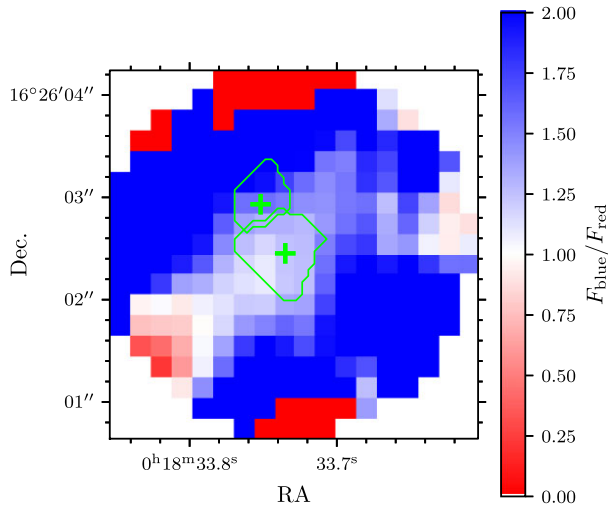
Figure 8. Blue-to-red peak ratio map for RXC0018-LAE1.2. The figure shows the three Kron radii area extracted from the continuum-subtracted MUSE cube (see Section 4.1). The green crosses and curves show the *HST* continuum centroids and segmentations, respectively, like in Fig. 4.

The most prominent feature of this Ly α emission profile is that the blue peak is significantly stronger than the red peak with a blue-to-red peak ratio of 1.7 ± 0.1 (EW$_{\text{blue, 0}} = 40 \pm 2$ Å and EW$_{\text{red, 0}} = 24 \pm 2$ Å). We show the spatial distribution of the peak ratios for RXC0018-LAE1.2 in Fig. 8, similarly to Erb, Steidel & Chen (2018). As could already be expected from the signal-to-noise curves shown in Fig. 3, the whole Ly α emission is dominated by the blue peak and the peak ratio becomes closer to unity towards the centroid of the emission where the slightly more compact red peak is also strongest. This is similar to what Erb et al. (2018) found, i.e. that the blue component becomes stronger towards the outer regions, even though it overall dominates the whole Ly α emission region in the case of RXC0018-LAE1. This blue-to-red peak ratio places RXC0018-LAE1 in stark contrast to other double-peaked LAEs observed to date. Indeed, the vast majority of double-peaked LAEs in large samples are dominated by their red peak (e.g. Leclercq et al. 2017; Erb et al. 2018; Izotov et al. 2018; Matthee et al. 2021; Kerutt et al. 2022; Naidu et al. 2022). In some rare individual cases both peaks are almost equal (e.g. Trainor et al. 2015; Leclercq et al. 2017; Izotov et al. 2018; Naidu et al. 2022), roughly equal but extremely faint (e.g. Erb et al. 2014), or a slightly stronger blue peak is located red-ward of the systemic redshift (Endsley et al. 2022). Note that several instances of double-peaked Ly α with stronger blue peaks have been detected in extended Ly α blobs (Vanzella et al. 2017; Erb et al. 2018; Ao et al. 2020; Li et al. 2022). In these cases the two Ly α peaks usually originate from distinct spatially separated objects or regions within the extended Ly α blob however, whereas both the blue and the red peak clearly originate from the same galaxy in RXC0018-LAE1 (see Fig. 3).

A dominant red peak is usually interpreted as evidence that the Ly α photons scatter through an outflowing medium (e.g. Dijkstra, Haiman & Spaans 2006; Verhamme, Schaerer & Maselli 2006; Barnes et al. 2011; Yang et al. 2014; Gronke & Dijkstra 2016; Gurung-López, Orsi & Bonoli 2019). The blue peak being stronger on the other hand could indicate an inflow of circumgalactic gas into the Ly α emitting galaxy (e.g. Dijkstra et al. 2006; Verhamme et al. 2006; Yang et al. 2014). Since gas accretion has been found to preferentially occur along filamentary streams (e.g. Kereš et al. 2005, 2009; Dekel et al. 2009), this could potentially imply low

covering fractions of neutral hydrogen and thus low H I column density channels which could also allow LyC photons to escape. This however also strongly depends on other parameters such as velocity and gas temperature (e.g. Kakiichi & Gronke 2021; Li & Gronke 2022). Another indication of possible LyC escape would be a detection of Ly α photons escaping in the valley between the peaks near the line centre (e.g. Dijkstra et al. 2016; Vanzella et al. 2016; Rivera-Thorsen et al. 2017; Gazagnes et al. 2020; Matthee et al. 2021; Naidu et al. 2022). While our spectra in Fig. 6 hint at a possible $f_\lambda > 0$ between the two peaks, the spectral resolution of the MUSE data is not sufficient to properly resolve this. It will therefore require further spectroscopic observations with very high spectral resolution to determine if this galaxy has Ly α photons escaping at the line centre.

5 GALAXY PROPERTIES

In order to place these Ly α results into context, we infer galaxy parameters by fitting SEDs to the broad-band photometry and emission line EWs with the `BayEsian Analysis of Galaxy sEds` tool (`BEAGLE`; Chevallard & Charlot 2016), which is optimized to probe a large parameter space using a Bayesian MCMC approach. We use stellar and nebular SED templates by Plat et al. (2019), which combine the latest version of the stellar population templates by Bruzual & Charlot (2003) with the photoionization code `CLOUDY` (Ferland et al. 2013), and account for IGM attenuation with absorption models by Inoue et al. (2014). Note that with the Plat et al. (2019) templates, the fraction $f_{\text{esc, LyC}}$ of LyC photons escaping from density-bounded H II regions is a free parameter in our SED-fit. This is important because $f_{\text{esc, LyC}} > 0$ can significantly affect the galaxy SED, weakening both nebular lines and continuum emission (e.g. Zackrisson et al. 2013, 2017). The latter in particular also tends to make the galaxy SED bluer in the UV which might account for the extremely steep UV-slopes that we find (see Section 4.2).

The fit is performed for the main component of RXC0018-LAE1 for which we use the magnification-corrected photometry of RXC0018-7338 and the optical EWs measured in Section 3. Since neither Ly α nor IGM radiative transfer are straightforward to model, we exclude the measured Ly α EW and the three bluest filters ($F435W$, $F555W$, and $F606W$) from the fit. We assume a delayed star-forming history, which goes as $\psi(t) \propto t\exp(-t/\tau)$, with the possibility for an ongoing star-burst for the last 10 Myr and model the dust attenuation using an SMC-like dust extinction law (Pei 1992) which has been found to well fit star-forming galaxies at $z \sim 3$ (e.g. Reddy et al. 2018a), in particular at low metallicities (Shivaei et al. 2020). The best-fitting maximum-a-posteriori (MAP) SED is shown in Fig. 9 and the fit results in a low stellar mass of $\log(M_\star/M_\odot) = 7.50^{+0.34}_{-0.21}$, a stellar age of $\log(t_{\text{age}}/\text{yr}) = 8.66^{+0.37}_{-0.48}$, and a moderate current star formation rate $\log(\psi/M_\odot \text{ yr}^{-1}) = 0.18^{+0.02}_{-0.02}$. These results again place RXC0018-LAE1 apart from the EELGs typically considered as high-redshift analogues (see Section 3) with very young ages and extreme ongoing star formation activity (e.g. Atek et al. 2011, 2014; Maseda et al. 2014, 2018; Reddy et al. 2018b; Tang et al. 2019; Boyett et al. 2022). The low metallicity and dust attenuation optical depth that we find, $\log(Z/Z_\odot) = -0.99^{+0.24}_{-0.13}$ and $\hat{\tau}_V = 0.009^{+0.010}_{-0.006}$, are however in line with what can be expected for a high-redshift analogue. The posterior distribution of our SED-fit predicts relatively high LyC escape fractions of $f_{\text{esc, LyC}} > 0.7$ at 3σ because these models provide the best interpretation of the low optical emission line EWs and the extremely blue UV-slopes that we measure (see Sections 3 and 4.2). Note that the galaxy parameters inferred above and the
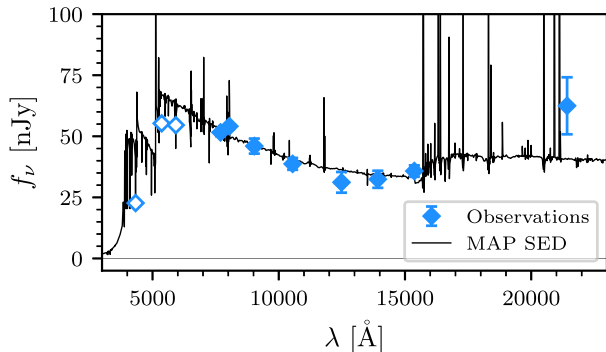
Figure 9. Best-fitting `BEAGLE` SED for RXC0018-LAE1. The magnification-corrected photometry is shown as blue diamonds. The solid data points represent filters used in the fit and the open points the filters excluded. The black curve represents the maximum-a-posteriori spectrum predicted by `BEAGLE`.

optical emission features presented in Section 3 make RXC0018-LAE1 similar to another $z \sim 3$ source observed by Shapley et al. (2016), which has a direct LyC detection and a relatively high inferred LyC escape fraction >0.5.

6 CONCLUSION

In this work, we report the detection of a multiply imaged double-peaked LAE in the MUSE coverage of the RELICS cluster RXC J0018.5+1626, dubbed RXC0018-LAE1. Unlike most observed double-peaked LAEs, this object shows a peculiar Ly α emission profile dominated by its blue peak rather than the red peak. To the best of our knowledge, this is the first observed object showing this kind of Ly α profile at moderate redshifts to date. Using the rest-frame optical [O III] and H β emission lines we find the systemic redshift of this object to be $z_{\rm sys} = 3.2177 \pm 0.0001$. Throughout our analysis of RXC0018-LAE1, we find this galaxy to have numerous properties that set it apart from typical LAEs and might indicate it to also leak LyC photons. These properties are:

(i) A unique double-peaked Ly α emission profile in which the blue peak is stronger than the red peak by a blue-to-red ratio of 1.7 ± 0.1.

(ii) Possible escape of Ly α photons at the line centre.

(iii) A relatively large Ly α EW of EW$_0$ = (63 ± 2) Å and luminosity of $L_{\rm Ly\alpha} = (6.7 \pm 0.5) \times 10^{42} \, \rm erg \, s^{-1}$.

(iv) Extremely blue UV continuum slopes and in particular a flattening towards the FUV with $\beta_{\rm NUV} = -3.0 \pm 0.2$ and $\beta_{\rm FUV} = -2.23 \pm 0.06$.

(v) Relatively low optical nebular line EWs, EW$_0 = (159 \pm 51)$ Å for [O III] $\lambda 5007$ Å and EW$_0$ = (33 ± 12) Å for H β, an [O III] $\lambda 5007$ Å/H β ratio of 4.8 ± 0.7, and a non-detection of the [O II] doublet resulting in a 3σ lower limit on the [O III]/[O II] ratio of >9.3.

(vi) An SED-fit with `BEAGLE` that shows a low stellar mass $\log(M_\star / \rm M_\odot) = 7.50^{+0.34}_{-0.21}$, a very low dust attenuation $\hat{\tau}_V = 0.009^{+0.010}_{-0.006}$ and predicts LyC escape fractions of $f_{\rm esc, \, LyC} > 0.7$.

Given these properties, RXC0018-LAE1 is an interesting target to observe in wavelengths bluer than the Lyman-limit 912 Å (<3765 Å at $z = 3.218$) in order to directly detect its LyC emission and constrain the escape fraction with, e.g. deep *HST* UV imaging. Further deep high-resolution spectroscopy will also be needed both to resolve the main component's Ly α emission at the line centre,

to further constrain its rest-frame UV emission lines, and to study the two smaller objects in order to determine (i) if they are indeed companions to RXC0018-LAE1 at the same redshift and (ii) how they dynamically interact and how this affects the LyC escape. It is possible that the interaction with the companion galaxies facilitates low H I column density channels crucial to LyC escape. It would therefore also be beneficial to study the circumgalactic medium of RXC0018-LAE1 with different diagnostics than the resonant Ly α line such as e.g. rest-frame far-infrared (FIR) lines redshifted to *Atacama Large Millimeter/submillimeter Array* (ALMA) bandpass at $z \simeq 3.218$. The high magnification factors ($\mu \sim 7$–10) and image multiplicity, which allows us to stack observations of both images to gain additional depth, make RXC0018-LAE1 a prime target for deep follow-up observations to study a strong candidate LyC leaking, low-mass high-redshift galaxy analogue.

---

[4]http://www.astropy.org

DATA AVAILABILITY

The RELICS *HST* data and catalogues on which this work is based are publicly available on the MAST archive in the RELICS repository for RXC0018.[2] The VLT HAWK-I and MUSE data are publicly available on the ESO Science Archive[3] under program IDs 0103.A-0871(B) and 0103.A-0777(B), respectively. Finally, the Gemini/GNIRS data and lensing models used in this work will be shared by the authors on request.

REFERENCES

Amorín R., Pérez-Montero E., Vílchez J. M., Papaderos P., 2012, ApJ, 749, 185
Ao Y. et al., 2020, Nat. Astron., 4, 670
Astropy Collaboration, 2013, A&A, 558, A33
Atek H. et al., 2011, ApJ, 743, 121
Atek H. et al., 2014, ApJ, 789, 96
Atek H. et al., 2015, ApJ, 814, 69
Bacon R. et al., 2010, in McLean I. S., Ramsay S. K., Takami H., eds, Proc.SPIE Conf. Ser. Vol. 7735, Ground-based and Airborne Instrumentation for Astronomy III. SPIE, Bellingham, p. 773508
Bañados E. et al., 2019, ApJ, 885, 59
Barnes L. A., Haehnelt M. G., Tescari E., Viel M., 2011, MNRAS, 416, 1723
Bassett R. et al., 2019, MNRAS, 483, 5223
Becker G. D., Bolton J. S., Madau P., Pettini M., Ryan-Weber E. V., Venemans B. P., 2015, MNRAS, 447, 3402
Benítez N., 2000, ApJ, 536, 571
Bertin E., Arnouts S., 1996, A&AS, 117, 393
Bian F., Fan X., 2020, MNRAS, 493, L65
Bosman S. E. I. et al., 2022, MNRAS, 514, 55
Bouwens R. J. et al., 2009, ApJ, 705, 936
Bouwens R. J. et al., 2011, ApJ, 737, 90
Bouwens R. J. et al., 2015, ApJ, 803, 34
Boyett K. N. K., Stark D. P., Bunker A. J., Tang M., Maseda M. V., 2022, MNRAS, 513, 4451
Bradley L. et al., 2021, astropy/photutils: 1.3.0. doi:10.5281/zenodo.5796924, https://doi.org/10.5281/zenodo.5796924
Bruzual G., Charlot S., 2003, MNRAS, 344, 1000
Bunker A. J. et al., 2010, MNRAS, 409, 855
Cai Z. et al., 2018, ApJ, 861, L3
Cantalupo S. et al., 2019, MNRAS, 483, 5188
Cardamone C. et al., 2009, MNRAS, 399, 1191
Chevallard J., Charlot S., 2016, MNRAS, 462, 1415
Coe D., Benítez N., Sánchez S. F., Jee M., Bouwens R., Ford H., 2006, AJ, 132, 926
Coe D. et al., 2019, ApJ, 884, 85
Dekel A. et al., 2009, Nature, 457, 451
Dijkstra M., Haiman Z., Spaans M., 2006, ApJ, 649, 14
Dijkstra M., Gronke M., Venkatesan A., 2016, ApJ, 828, 71
Drake A. B. et al., 2017a, MNRAS, 471, 267
Drake A. B. et al., 2017b, A&A, 608, A6
Earl N. et al., 2021, astropy/specutils: V1.5.0. doi:10.5281/zenodo.5721652, https://doi.org/10.5281/zenodo.5721652
Ebeling H., Barrett E., Donovan D., Ma C.-J., Edge A. C., van Speybroeck L., 2007, ApJ, 661, L33
Endsley R. et al., 2022, preprint (arXiv:2202.01219)
Erb D. K. et al., 2014, ApJ, 795, 33
Erb D. K., Steidel C. C., Chen Y., 2018, ApJ, 862, L10
Ferland G. J. et al., 2013, Rev. Mex. Astron. Astrofis., 49, 137
Finkelstein S. L. et al., 2015, ApJ, 810, 71
Fletcher T. J., Tang M., Robertson B. E., Nakajima K., Ellis R. S., Stark D. P., Inoue A., 2019, ApJ, 878, 87

Flury S. R. et al., 2022a, ApJS, 260, 1
Flury S. R. et al., 2022b, ApJ, 930, 126
Foreman-Mackey D., Hogg D. W., Lang D., Goodman J., 2013, PASP, 125, 306
Fuller S. et al., 2020, ApJ, 896, 156
Furtak L. J., Atek H., Lehnert M. D., Chevallard J., Charlot S., 2021, MNRAS, 501, 1568
Gazagnes S., Chisholm J., Schaerer D., Verhamme A., Izotov Y., 2020, A&A, 639, A85
Ginsburg A., Robitaille T., Beaumont C., ZuHone J., 2014, Release Candidate 2 - Includes yt Interop. doi:10.5281/zenodo.11485, https://doi.org/10.5281/zenodo.11485
Goto H. et al., 2021, ApJ, 923, 229
Gronke M., Dijkstra M., 2016, ApJ, 826, 14
Gurung-López S., Orsi Á. A., Bonoli S., 2019, MNRAS, 490, 733
Hashimoto T. et al., 2017, A&A, 608, A10
Hayashino T. et al., 2004, AJ, 128, 2073
Henry A., Scarlata C., Martin C. L., Erb D., 2015, ApJ, 809, 19
Herenz E. C., Wisotzki L., 2017, A&A, 602, A111
Hu E. M., Cowie L. L., Songaila A., Barger A. J., Rosenwasser B., Wold I. G. B., 2016, ApJ, 825, L7
Hu W. et al., 2019, ApJ, 886, 90
Hunter J. D., 2007, Comput. Sci. Eng., 9, 90
Inoue A. K., Shimizu I., Iwata I., Tanaka M., 2014, MNRAS, 442, 1805
Izotov Y. I., Guseva N. G., Thuan T. X., 2011, ApJ, 728, 161
Izotov Y. I., Schaerer D., Thuan T. X., Worseck G., Guseva N. G., Orlitová I., Verhamme A., 2016, MNRAS, 461, 3683
Izotov Y. I., Thuan T. X., Guseva N. G., 2017, MNRAS, 471, 548
Izotov Y. I., Worseck G., Schaerer D., Guseva N. G., Thuan T. X., Fricke, Verhamme A., Orlitová I., 2018, MNRAS, 478, 4851
Izotov Y. I., Worseck G., Schaerer D., Guseva N. G., Chisholm J., Thuan T. X., Fricke K. J., Verhamme A., 2021, MNRAS, 503, 1734
Jaskot A. E., Oey M. S., 2013, ApJ, 766, 91
Jaskot A. E., Dowd T., Oey M. S., Scarlata C., McKinney J., 2019, ApJ, 885, 96
Jullo E., Kneib J.-P., 2009, MNRAS, 395, 1319
Jullo E., Kneib J.-P., Limousin M., Elíasdóttir Á., Marshall P. J., Verdugo T., 2007, New J. Phys., 9, 447
Kakiichi K., Gronke M., 2021, ApJ, 908, 30
Kereš D., Katz N., Weinberg D. H., Davé R., 2005, MNRAS, 363, 2
Kereš D., Katz N., Fardal M., Davé R., Weinberg D. H., 2009, MNRAS, 395, 160
Kerutt J. et al., 2022, A&A, 659, A183
Kissler-Patig M. et al., 2008, A&A, 491, 941
Kneib J.-P., Ellis R. S., Smail I., Couch W. J., Sharples R. M., 1996, ApJ, 471, 643
Kron R. G., 1980, ApJS, 43, 305
Leclercq F. et al., 2017, A&A, 608, A8
Leclercq F. et al., 2020, A&A, 635, A82
Li Z., Gronke M., 2022, MNRAS, 513, 5034
Li Z., Steidel C. C., Gronke M., Chen Y., Matsuda Y., 2022, MNRAS, 513, 3414
Madau P., 1995, ApJ, 441, 18
Mahler G. et al., 2019, ApJ, 873, 96
Maji M. et al., 2022, A&A, 663, A66
Marchi F. et al., 2018, A&A, 614, A11
Maseda M. V. et al., 2014, ApJ, 791, 17
Maseda M. V. et al., 2018, ApJ, 854, 29
Matthee J., Sobral D., Gronke M., Paulino-Afonso A., Stefanon M., Röttgering H., 2018, A&A, 619, A136
Matthee J. et al., 2021, MNRAS, 505, 1382
McLure R. J. et al., 2013, MNRAS, 432, 2696
Meyer R. A., Laporte N., Ellis R. S., Verhamme A., Garel T., 2021, MNRAS, 500, 558
Momose R. et al., 2014, MNRAS, 442, 110
Momose R. et al., 2016, MNRAS, 457, 2318
Naidu R. P., Forrest B., Oesch P. A., Tran K.-V. H., Holden B. P., 2018, MNRAS, 478, 791

---

[2]https://archive.stsci.edu/missions/hlsp/relics/rxc0018 + 16/
[3]http://archive.eso.org/scienceportal/home

Naidu R. P., Tacchella S., Mason C. A., Bose S., Oesch P. A., Conroy C., 2020, ApJ, 892, 109

Naidu R. P. et al., 2022, MNRAS, 510, 4582

Ofek E. O., 2014, Astrophysics Source Code Library, record ascl:1407.005

Oke J. B., Gunn J. E., 1983, ApJ, 266, 713

Pahl A. J., Shapley A., Faisst A. L., Capak P. L., Du X., Reddy N. A., Laursen P., Topping M. W., 2020, MNRAS, 493, 3194

Pahl A. J., Shapley A., Steidel C. C., Chen Y., Reddy N. A., 2021, MNRAS, 505, 2447

Pei Y. C., 1992, ApJ, 395, 130

Pentericci L. et al., 2014, ApJ, 793, 113

Pentericci L. et al., 2018, A&A, 619, A147

Planck Collaboration XLVII, 2016, A&A, 596, A108

Planck Collaboration VI, 2020, A&A, 641, A6

Plat A., Charlot S., Bruzual G., Feltre A., Vidal-García A., Morisset C., Chevallard J., Todt H., 2019, MNRAS, 490, 978

Price-Whelan A. M. et al., 2018, AJ, 156, 123

Reddy N. A., Steidel C. C., Pettini M., Bogosavljević M., Shapley A. E., 2016, ApJ, 828, 108

Reddy N. A. et al., 2018a, ApJ, 853, 56

Reddy N. A. et al., 2018b, ApJ, 869, 92

Rivera-Thorsen T. E. et al., 2017, A&A, 608, L4

Robertson B. E., 2021, preprint (arXiv:2110.13160)

Robertson B. E. et al., 2013, ApJ, 768, 71

Robertson B. E., Ellis R. S., Furlanetto S. R., Dunlop J. S., 2015, ApJ, 802, L19

Schaerer D., Izotov Y. I., Nakajima K., Worseck G., Chisholm J., Verhamme A., Thuan T. X., de Barros S., 2018, A&A, 616, L14

Schaerer D. et al., 2022, A&A, 658, L11

Schenker M. A., Ellis R. S., Konidaris N. P., Stark D. P., 2014, ApJ, 795, 20

Shapley A. E., Steidel C. C., Strom A. L., Bogosavljević M., Reddy N. A., Siana B., Mostardi R. E., Rudie G. C., 2016, ApJ, 826, L24

Shivaei I. et al., 2020, ApJ, 899, 117

Songaila A., Hu E. M., Barger A. J., Cowie L. L., Hasinger G., Rosenwasser B., Waters C., 2018, ApJ, 859, 91

Stark D. P., Ellis R. S., Chiu K., Ouchi M., Bunker A., 2010, MNRAS, 408, 1628

Stasińska G., Izotov Y., Morisset C., Guseva N., 2015, A&A, 576, A83

Steidel C. C., Bogosavljević M., Shapley A. E., Kollmeier J. A., Reddy N. A., Erb D. K., Pettini M., 2011, ApJ, 736, 160

Steidel C. C., Bogosavljević M., Shapley A. E., Reddy N. A., Rudie G. C., Pettini M., Trainor R. F., Strom A. L., 2018, ApJ, 869, 123

Tang M., Stark D. P., Chevallard J., Charlot S., 2019, MNRAS, 489, 2572

Trainor R. F., Steidel C. C., Strom A. L., Rudie G. C., 2015, ApJ, 809, 89

van der Walt S., Colbert S. C., Varoquaux G., 2011, Comput. Sci. Eng., 13, 22

Vanzella E. et al., 2016, ApJ, 821, L27

Vanzella E. et al., 2017, MNRAS, 465, 3803

Vanzella E. et al., 2018, MNRAS, 476, L15

Verhamme A., Schaerer D., Maselli A., 2006, A&A, 460, 397

Verhamme A., Orlitová I., Schaerer D., Hayes M., 2015, A&A, 578, A7

Verhamme A., Orlitová I., Schaerer D., Izotov Y., Worseck G., Thuan T. X., Guseva N., 2017, A&A, 597, A13

Verhamme A. et al., 2018, MNRAS, 478, L60

Virtanen P. et al., 2020, Nat. Methods, 17, 261

Vitral E., 2021, MNRAS, 504, 1355

Wisotzki L. et al., 2016, A&A, 587, A98

Wisotzki L. et al., 2018, Nature, 562, 229

Wold I. G. B. et al., 2022, ApJ, 927, 36

Yang Y., Zabludoff A., Jahnke K., Davé R., 2014, ApJ, 793, 114

Zackrisson E., Rydberg C.-E., Schaerer D., Östlin G., Tuli M., 2011, ApJ, 740, 13

Zackrisson E., Inoue A. K., Jensen H., 2013, ApJ, 777, 39

Zackrisson E. et al., 2017, ApJ, 836, 78

Zhu Y. et al., 2021, ApJ, 923, 223

Zitrin A. et al., 2009, MNRAS, 396, 1985

Zitrin A., Broadhurst T., Barkana R., Rephaeli Y., Benítez N., 2011, MNRAS, 410, 1939

Zitrin A. et al., 2015, ApJ, 801, 44

APPENDIX A: SEARCH FOR FURTHER EMISSION LINES

Our GNIRS and MUSE spectra yielded clear detections of the [O III], H β, and Ly α lines in RXC0018-LAE1, respectively, as described in Sections 3 and 4. In addition to those, we search the spectra for other emission lines at the wavelengths where they can be expected given the systemic redshift $z_{sys} = 3.2177 \pm 0.0001$. We derive upper limits and some tentative detections as described in the following sections. Because of their weak signal-to-noise however, we defer a detailed analysis of these possible emission features to future work with deeper spectroscopic observations.

A1 The [O II] doublet upper limit in GNIRS

The H-band spectrum of our GNIRS observations of RXC0018-7203 is shown in Fig. A1. While it contains many sky lines, the spectral region where we may expect the [O II] $\lambda\lambda3726$ Å,3729 Å doublet at $z \simeq 3.218$, $\lambda \simeq 15716$ Å, and $\lambda \simeq 15729$ Å is relatively free. None the less, we do not detect any significant flux at the expected location of the [O II] doublet. Integrating the variance spectrum in a 30 Å window around the expected wavelengths, we measure the 1σ upper limit on the total magnification-corrected flux and the rest-frame EW using the H-band photometry given in Table 1. The upper limits are shown in Table A1.

A2 Rest-frame UV lines in MUSE

In order to search for additional rest-frame UV emission lines beyond the prominent double-peaked Ly α feature in RXC0018-LAE1, we carefully inspect the entire spectral axis of the MUSE cube. A particular criterion for this is that the potential emission features appear consistently in both multiple images. We tentatively find some weak emission in both images at the expected wavelengths of the C IV $\lambda\lambda1548$ Å,1551 Å and C III] $\lambda\lambda1907$ Å,1909 Å doublets and
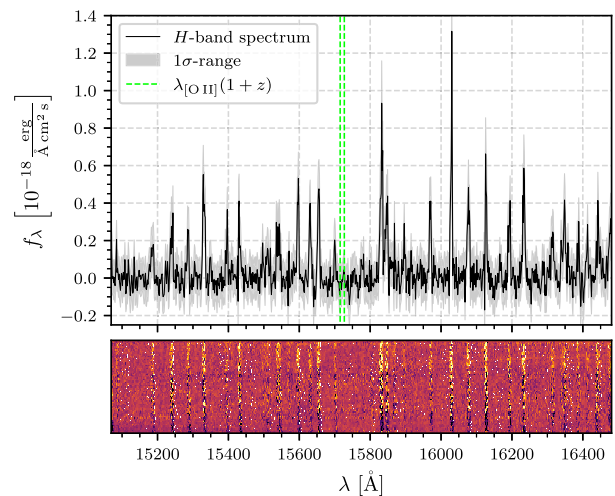

Figure A1. Observed GNIRS H-band spectrum of RXC0018-7203 (black) and its 1σ-range (grey shaded area). The green dashed lines show where the [O II] $\lambda\lambda3726$ Å,3729 Å doublet can be expected given the spectroscopic redshift of RXC0018-LAE1 measured with the K-band lines.

Table A1. Rest-frame UV spectroscopy results for RXC0018-LAE1 measured in the MUSE and GNIRS data. The integrated line fluxes were corrected for the gravitational magnification given in Table 1. In the case of non-detections, we quote 1σ upper limits here. The $\frac{F_{\mathrm{line}}}{\Delta F_{\mathrm{line}}}$ columns contain integrated signal-to-noise ratios.

| Line	RXC0018-LAE1.1				RXC0018-LAE1.2		
	λ_{obs} [Å]	F_{line} [10^{-18} erg s^{-1} cm^{-2}]	EW$_0$ [Å]	$\frac{F_{\mathrm{line}}}{\Delta F_{\mathrm{line}}}$	F_{line} [10^{-18} erg s^{-1} cm^{-2}]	EW$_0$ [Å]	$\frac{F_{\mathrm{line}}}{\Delta F_{\mathrm{line}}}$
Si IV λ1394 Å	–	<0.26	<0.9	–	<0.15	<0.8	–
Si IV λ1403 Å	–	<0.26	<0.9	–	<0.14	<0.7	–
C IV λ1548 Å	6525.6 ± 0.5	0.40 ± 0.10	1.7 ± 0.4	4.0	0.45 ± 0.08	2.8 ± 0.5	5.6
C IV λ1551 Å	6531.2 ± 1.7	<0.10	<0.4	–	0.19 ± 0.07	1.2 ± 0.5	2.7
He II λ1640 Å	6913.4 ± 0.4	0.37 ± 0.10	1.7 ± 0.5	3.7	0.47 ± 0.07	3.6 ± 0.4	6.7
O III] λ1661 Å	–	<0.14	<0.7	–	<0.09	<0.7	–
O III] λ1666 Å	–	<0.14	<0.7	–	<0.08	<0.6	–
C III] λ1907 Å	8036.4 ± 0.3	0.42 ± 0.08	2.7 ± 0.5	5.3	0.62 ± 0.08	6.2 ± 0.6	7.8
C III] λ1909 Å	8045.1 ± 0.4	0.39 ± 0.07	2.5 ± 0.5	5.6	0.42 ± 0.06	4.2 ± 0.6	7.0
[O II] $\lambda\lambda$3726, 3729 Å	–	<0.07	<2.3	–	–	–	–
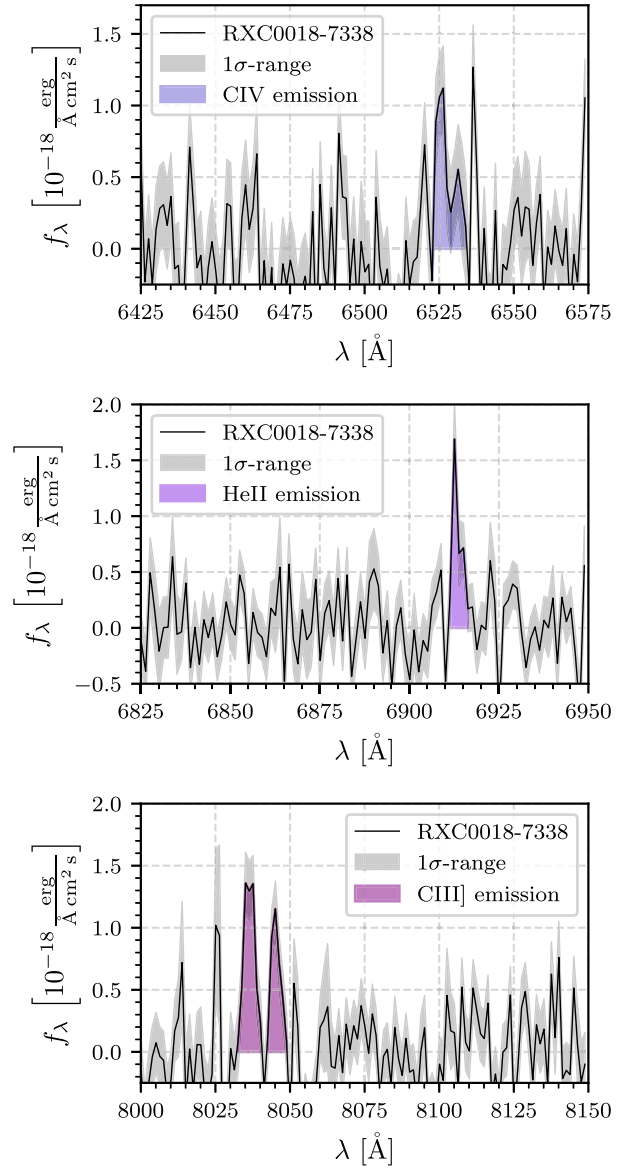
Figure A2. Continuum-subtracted C IV (*top panel*), He II (*middle panel*), and C III] (*bottom panel*) emission in RXC0018-7338. The colour shaded areas represent the integrated line fluxes and the grey shaded area represents the 1σ-range of the observed spectra.

the He II λ1640 Å line. We do not find the Si IV $\lambda\lambda$1394 Å,1403 Å and O III] $\lambda\lambda$1661 Å,1666 Å doublets where expected given the systemic redshift of our target however. We also do not find any significant emission lines for the tertiary component (IDs 7315 and 7495) consistently over both images.

We extract circular regions of the diameter of the MUSE PSF FWHM (see Fig. 3) around the main component of RXC0018-LAE1 (i.e. RXC0018-7203 and RXC0018-7338) from the continuum-subtracted MUSE cube constructed in Section 4.1 and collapse them to 1D spectra. We then use the same methods as described in Sections 3 and 4.3 to measure line centres, integrated flux, and rest-frame EWs of these lines. The measured properties can be found in Table A1 and we show the C IV, He II, and C III] spectra of RXC0018-7338 in Fig. A2. We measure upper limits for the lines that we do not detect by integrating the variance spectrum in a 20 Å window around the expected line position. The EWs in Table A1 are computed

using the UV-continuum fits obtained in Section 4.2 to estimate the continuum.

As is apparent from the values in Table A1, these detections are very weak. Indeed, the peak flux density barely exceeds 2σ, in particular for the C IV lines (i.e. the integrated flux might be higher as can be seen in Table A1, but the flux density in each spectral element does not exceed $\sim 2\sigma$). A recent study of low-redshift LyC leakers has established a tentative connection between the LyC escape fraction and the C IV/C III]-doublet flux ratio (Schaerer et al. 2022). Summing the fluxes of each doublet, we find a C IV/C III]-ratio of 0.6 ± 0.1 based on the measurement for RXC0018-LAE1.2 (see Table A1), which is just below the ratios typically found for strong LyC leakers in Schaerer et al. (2022), i.e. $\gtrsim 0.7$. Note that this estimate is based on only three galaxies though and given the uncertainties in both our and the Schaerer et al. (2022) measurements, a high LyC escape fraction would still be consistent in RXC0018-LAE1. Moreover, as can be seen in Fig. A2, our detections are rather tentative though, in particular that of C IV $\lambda 1551\,\text{Å}$, even in the more magnified image. We will therefore need deeper spectroscopy to obtain more robust detections to better measure this ratio. Note that the same study by Schaerer et al. (2022) found the presence of He II $\lambda 1640\,\text{Å}$ to also correlate with LyC escape since it indicates a strong ionization field.

Interestingly, the He II $\lambda 1640\,\text{Å}$ seems to be spatially shifted towards the secondary component (IDs 7202 and 7338) in both multiple images. While the effective spatial resolution of the MUSE data (see e.g. Fig. 3 for the FWHM of the MUSE PSF) does not allow us to properly resolve the exact spatial origin of the emission line, this might none the less indicate that the He II emission actually originates from the secondary component rather than the main component like the other emission lines measured in this work. If this were indeed the case, it would place the secondary component at a spectroscopic redshift $z = 3.2156 \pm 0.0003$, which would make it a close companion to the Ly α-emitting galaxy. Note that the difference between this measurement and the systemic redshift of the main component is not sufficient to account for the peak separation of the Ly α emission. Our previous conclusions that the double-peaked Ly α originates from one and the same object, the main component of RXC0018-LAE1, are therefore not contradicted by this detection. We will need deeper observations with higher spectral and spatial resolution to robustly detect these tentative emission lines, measure their properties, and determine if the He II emission indeed originates from the secondary component.

This paper has been typeset from a TEX/LATEX file prepared by the author.